Thermo-mechanical modelling to evaluate residual stress and material compatibility of laser cladding process depositing similar and dissimilar material on Ti6Al4V alloy

N. Tamanna [*], I.R. Kabir, S. Naher

School of Mathematics, Computer Science and Engineering, City, University of London, United Kingdom

ABSTRACT

The formation of residual stresses due to thermo-mechanical effect and microstructural transformation in the Laser Cladding process predominantly affects the final product integrity and service life. A 3D finite element transient thermo-mechanical model has been developed to predict thermal profile and residual stress distribution for repair application of Ti6Al4V alloy using a moving heat source. Then the developed model was applied for the deposition of ceramic materials Al_2O_3 and TiC on Ti6Al4V alloy substrate. The outcome of this model is to predict temperature distribution, cooling rate, melt pool depth, heat affected zone and residual stress. This study mainly highlights the thermal effect on the residual stresses for similar and dissimilar clad/substrate materials and suggests the suitable cladding material with minimum residual stress.

Introduction

The Laser Cladding (LC) process directs a high-intensity laser heat source to deposit a thin layer (from μm to mm) of metal/ceramic materials on a solid substrate to repair or enhance the substrate surface properties [1]. In the late 1970s, the Rockwell International Corporation successfully used the LC process to deposit ceramic powders on the metallic substrate, which significantly changed the future repair and coating industries. Since then, this process has become invaluably popular to coat numerous metallic and ceramic powders [2]. The common clad/coating materials are stainless steel, Ti6Al4V, H13 tool steel, stellite 6, Al_2O_3, TiC, WC, cobalt-based alloy, aluminium based alloy and Inconel 718 [3-12]. The substrate materials mainly comprise stainless steel, Ti6Al4V, low carbon steel, mild steel, medium carbon steel, and Inconel 718. The selection of clad materials for a specific substrate material is crucial to determining the compatibility between clad and substrate material for specific applications and required properties [13-15]. The mismatch of thermal properties and large thermal gradient between the clad and substrate introduces residual stresses in the deposited layer and heat-affected zone (HAZ), which causes dimensional inaccuracy, cracking, distortion, and immature failure of the components [16-18].

Simulation and modelling have become an efficient tool in research to understand the nature and reason of formation residual stresses during the LC process. Researchers developed several thermo-mechanical models of laser melting processes to predict induced residual stresses using ANSYS, ANSYS-CFD, ABAQUS, and FLUENT multi-physics platforms. Thermo-mechanical models usually have two parts: thermal and structural. The outcome of the thermal model is to predict temperature distribution, peak temperature, heating and cooling rates, HAZ, optimisation of laser power and the effect of process parameters during operation. For example, Guo et al. proposed a 3D thermal model of preplaced powder process to observe the effect of laser power on the melting of cladding and substrate materials [10]. In this model, a laser heat source scanned over a preplaced powder bed of cladding material on the substrate. This model provided a range of laser power (240 W–530 W) for proper melting of clad material and claimed that there would be a lack of fusion below 240 W and material will be vaporised above 530 W laser power leading to poor clad quality. Another model showed that the increment of laser power from 2500 W to 3000 W could increase the dilution from 6.25% to 33.75% [13].

The development of a thermal model of the coaxial powder system was relatively complicated as powder flows along the same axis of the laser heat source during the process. Therefore, the birth and kill technique uses to deposit clad materials on the substrate. In this technique, initially, all elements were killed in the clad area before applying heat source and then deactivated elements remained in the process with near-zero conductivity. Then the killed elements were activated specifically where the heat source was applied. Hao et al. developed a 3D thermal

---

Nomenclature

LC	Laser Cladding
HAZ	Heat-affected Zone
SLM	Selective Laser Melting
C_P	The specific heat (J/kg.K)
C_S	Specific heat capacity of solid
C_L	Specific heat capacity of liquid
C^*	Modified specific heat
T	Time dependent temperature
T_S	The solidus temperature
T_L	The liquidus temperature
∂T	The particle temperature variation in the time ∂t (K)
T_β	The beta transus temperature
k	Thermal conductivity (W/m•K)

L	The latent heat of fusion (J/kg)
P	Laser power
Q	The heat flux from laser heat source (W/m2)
R	Radius of the laser beam (m)
r	Distribution of heat source (m)
X, Y and Z	The three dimensions of a Cartesian coordinate system
t	Time (s)
∂t	Small variation of time (s)
SX, SY, SZ	The residual stress distribution in X, Y and Z directions
SEQV	The equivalent / von-Mises stress
d_p, d_a	Simulated and actual melt pool depth, respectively
$\varepsilon^{el}, \varepsilon^{pl}, \varepsilon^{th}$	Elastic, plastic, thermal strains, respectively
η	Absorption coefficient of material
ρ	Density (kg/m3)

model of the coaxial powder system to deposit a single clad layer [11]. This model was applied to predict temperature distribution with varying laser power, laser scanning speed and powder feed rate. Another study of the coaxial powder system showed that with increasing laser power 500 W, the peak temperature increased by 249 °C [19]. The 3D model developed by Farahmand et al. calculated the cooling rates at various preheating temperatures of the substrate [20]. The cooling rates in the clad decreased from 1800 °C/s to 960 °C/s with increasing the pre-heating temperature from room temperature to 300 °C. Then several thermal models were published to predict temperature distribution for double-track [21], multi-track [5,8,16] and overlapped clad [22]. A comprehensive 3D multi-physics finite element thermal model of coaxial powder-fed laser cladding investigated the heat transfer, fluid flow, shielding gas pressure, powder temperature-rise, surface tension, and free surface movement [23]. The results showed that the temperature gradient and undercooling at the solidification interface were significantly responsible for the crystal characteristic, while the solidification rate mainly governed the grain size. A similar numerical model investigated the internal convection morphology of the molten pool, which has an important influence on the solidification morphology of the deposited layer [24].

The thermal model is coupled with the structural model to predict residual stress distribution through modelling. Chew et al. developed a 3D model of the deposition AISI 4340 steel powder on a similar substrate material to predict residual stresses. The tensile residual stress was found in the clad, and the value was 953 MPa for single track deposition. The residual stress pattern in multi-track was similar to single-track deposition. However, the magnitude of residual stress reduced to 650 MPa due to post-heating during the cladding of the adjacent tracks [16]. Another model predicted residual stress for single and multi-track cladding of AISI H13 alloy on ASTM A36 substrate [8]. Both single and multi-track cladding layers showed a similar trend in residual stress generation. Maximum tensile residual stress was found in clad surface and the interface between clad and substrate, which reached 847 MPa for single track deposition and reduced for multi-track deposition. The internal compressive stress within the substrate complemented this tensile stress. In case of deposition of overlapped clad, maximum tensile residual stress was predicted at the interface of the substrate and clad, while it reduced with increasing the substrate temperature [25]. Additionally, the deposition of overlapped clad reduced the formation of cracks because the surface of previously formed clad got melted and reduced tensile residual stresses [26].

The high corrosion resistance, low density, and effective biological activity with heat resistance of Ti6Al4V alloys have made them the most outstanding choice in various industrial applications. However, their poor tribological properties inhibit utilising them in applications requiring abrasive and adhesive wear resistance [27]. Laser cladding

(LC) enhances the capabilities of such alloys by allowing the deposition of different hard coating with similar and dissimilar materials. Wang applied pure Ti coating on Ti-6Al-4 V alloys to improve the surface wear resistance. The hardness test showed that the coating has 433.82 HV, 30.4% harder than the Ti-6Al-4 V substrate. Besides, a lower wear volume in the coating than the substrate indicated improved wear resistance. In-depth analyses suggested that the improved surface performance could be mainly attributed to grain refinement strengthening in the clad zone [28]. However, the corrosion properties and strength of the similar metallic coating degrade in high-temperature applications. Oxide ceramics are particularly interested in such cases because of their low specific weight, low thermal conductivity, and good tribological properties [29]. Ceramic hard coatings like Al_2O_3, SiO, TiO2 and ZrO2 and other carbon-based ceramic (TiC) boost the high-temperature corrosion and wear properties, thermal insulation, improved surface finish. These are strongly recommended for engine and turbomachinery parts, including exhaust manifold and turbo housing [30]. In a previous analytical study, authors found that among four ceramic coatings (TiO2, TiC, ZrO2 and Al_2O_3), Al_2O_3 exhibits lower thermal strain when cladded on H13 tool steel sample [31]. Other experimental studies also evidenced the enhanced tribological corrosion properties of Al2O3 coating on Titanium [32], Magnesium [33] and others [34,35] alloys leading to high-temperature and biological applications. This article emphasises the Ti6Al4V alloys' wide acceptance in aerospace and biomedical applications. However, the brittleness of Al2O3 coating restricts any load-bearing applications. This area is still under-researched, although some researchers addressed this issue by alloying Al2O3 with other ceramic or metallic materials or composite coating. For example, Yao [36] and Chen [29] optimised the compositions of Al2O3 and TiO2 clad materials on Ti6Al4V substrate. Mthisi studied an admix of Ti and Al2O3 powder to clad Ti6Al4V alloy substrate [32]. A recent study developed a 3D numerical model of coaxial LC of Ti6Al4V titanium alloy deposited with tungsten carbide and nickel-based materials to study the thermal, microstructure, and clad layer geometry evolution [27].

Selecting appropriate hard ceramic coatings or optimising the composition of the ceramic coatings require extensive experimental efforts. This research addressed this issue by leveraging the competency of the modelling and simulation of LC that can be the best predictive tool in designating suitable coating materials for Ti6Al4V alloys in high temperature or biomedical applications. The authors notice that the past studies suggested alloyed or composite Al_2O_3 or TiC coatings for Ti64 alloys to improve the strength of the coating. However, the accurate prediction of the composition of the alloyed or composite coating materials requires appropriate materials properties. The existing material database or literature do not contain the material properties for those mixtures of the ceramic coating materials. Therefore, this study initiated
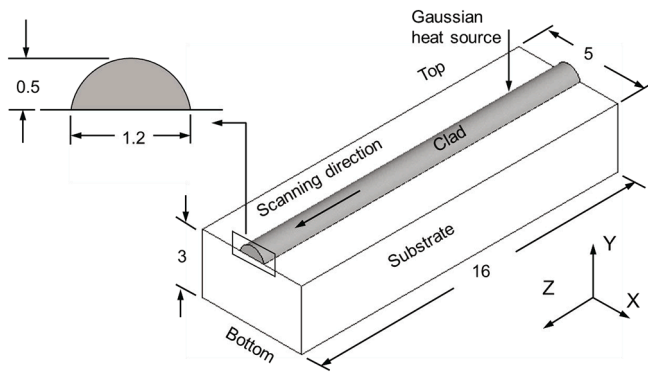
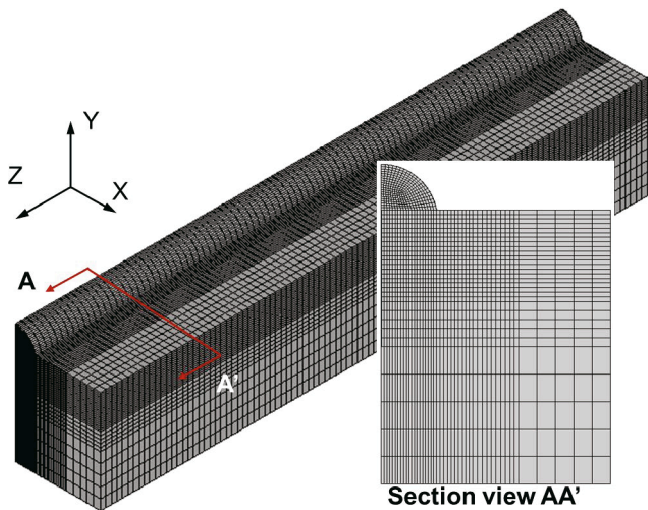**Fig. 1.** The geometry of 3D model. All dimensions are in mm.

Fig. 2. The meshing of the 3D symmetry model.

a 3D thermomechanical model of LC for Ti6Al4V alloy with single-component ceramic coating. The research first developed a 3D finite-element LC model for Ti6Al4V alloy with similar materials, verified it with an existing experimental study and extended it for Al$_2$O$_3$ and TiC separately, two different ceramic coatings. The results predict the thermal interaction of the materials with the substrate and residual stresses, giving insight into the reliability of applying hard ceramic coating on Ti6Al4V alloys in service. Additionally, this primitive model will provide information in developing an alloyed or composite ceramic coating model for the LC of Ti6Al4V alloys.

This research focuses on developing a 3D thermo-mechanical model of LC of Ti6Al4V alloy with similar material used in repair applications. This model predicts clad and substrate's thermal profile and residual stress distribution. Furthermore, the extension of the developed model follows for deposition of two ceramic materials, Al$_2$O$_3$ and TiC, on Ti6Al4V alloy substrate. The optimised laser power and laser beam diameter for the deposition of Al$_2$O$_3$ and TiC achieve complete melting in the clad and at the interface. The models predicted residual stresses and compared them for both materials. Comparing the predicted residual stresses of two ceramic materials systems can provide insight into selecting compatible clad/substrate materials with minimised residual stress in industrial applications. This study is an incremental attempt to develop predictive analyses of the LC process for Ti6Al4V alloy deposited with dissimilar materials, which uses two ceramic materials, Al$_2$O$_3$ and TiC, as starting materials.

Methodology: Thermomechanical modelling

3D geometry and meshing

In this study, ANSYS'19 Multiphysics software was used to develop the 3D thermo-mechanical model to predict thermal profile and residual stress distribution. The dimensions of the substrate were 110 mm length, 110 mm width and 13 mm height. The clad height and width were 0.5 mm and 1.2 mm respectively. The geometry was adopted from the experimental study of LC by Y. Sun et al. [37]. However, to reduce the computational cost, the dimensions of the substrate geometry was adjusted to 16 mm length, 5 mm width, and 3 mm height [11]. Fig. 1 shows the model consisting of the substrate and the clad.

The next step was 3D meshing, where half of the geometry was taken by considering the symmetry along the laser scanning direction (Z-direction) as shown in Fig. 2. For thermal analysis, the 3D Solid 70 hexahedron element was used which has 8 nodes with a single degree of freedom (temperature) at each node. Solid 70 element has a mechanical counterpart called Solid 185 element, which has three degrees of freedom at each node (translations in the nodal X, Y, and Z directions). For thermo-mechanical modelling, the thermal analysis was coupled with structural analysis and the Solid 70 element was switched to the Solid 185 during the modelling. The element birth and kill technique was used to replicate the deposition of clad material on the substrate. In this process, a heat source, which was a moving laser beam, was applied to melt the depositing powder material on the substrate. In case of applying heat source in the model, the elements of clad was killed and deactivated. As the laser progressed along the scanned region, the deactivated elements of the clad were activated gradually along with the moving heat source. The heat / temperature distribution of the heating source is mostly restricted in the clad region and a part of the substrate closer to the interface. Therefore, this area was meshed with finer elements compared to other parts. The rest of the substrate area was gradually meshed with coarser elements, as shown in Fig. 2. This is called the transitional mapped mesh technique [38,39], where a ratio between fine and coarse element size is followed for non-uniform mesh distribution. The non-uniform mesh distribution helps to minimise the number of elements and increases the computation speed, calculation accuracy of the temperature and residual stresses distributions. In the meshed model the total number of elements and nodes were counted 121,497 and 100900, respectively. The LC process is transient in nature; therefore, a transient coupled thermal and structure analysis was conducted in the model. The length of the time step was selected 1×10^{-3} s with a total time of 2.781 s to run the model.
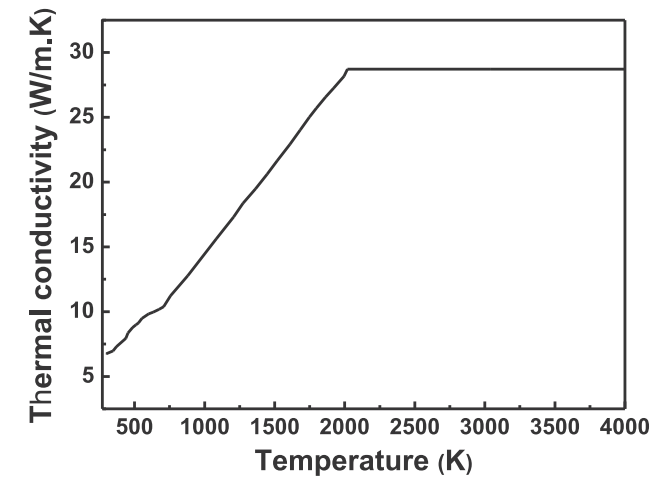
Material properties

At first, Ti6Al4V material was used as both substrate and clad material. The chemical composition of Ti6Al4V material is given in Table 1.

The solidus and liquidus temperatures of Ti6Al4V material are respectively around 1843 K and 1941 K. Therefore, there is a mushy zone of Ti6Al4V alloy. In order to calculate the temperature in this zone, latent heat of fusion was added in specific heat as a modified specific heat C* given in Equation (1)[11].
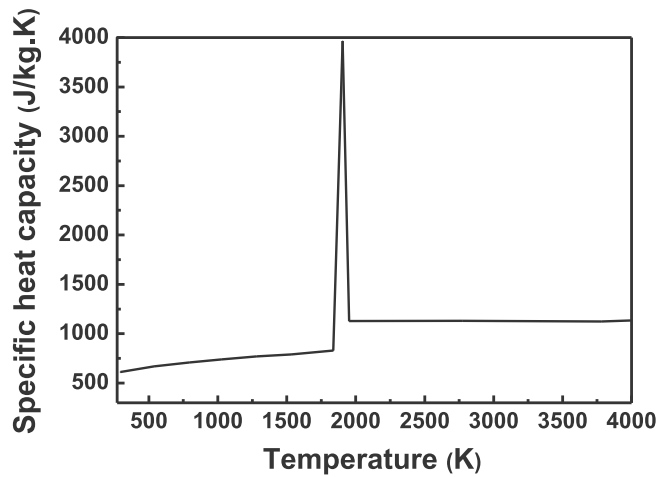
Table 1
The chemical composition of Ti6Al4V material [11].

Composition	Ti	O	Al	V	Fe	C	N	H	Other
Wt%	~89.438	0.09	6	4	0.04	0.02	0.01	0.002	⩽0.4

(a)

(b)

Fig. 3. Temperature dependent thermal properties (a) thermal conductivity and (b) specific heat capacity of Ti6Al4V alloy used in this model.

$$C^* = \frac{C_S(T) + C_L(T)}{2} + \frac{L}{T_L - T_S} T_S ⩽ T ⩽ T_L \tag{1}$$

where, C_S and C_L were specific heat capacity for the corresponding solid and liquid states of Ti6Al4V alloy, T_S and T_L were the solidus and the liquidus temperature, respectively. L was the latent heat of fusion which was 292 kJ/kg [11]. After reaching the melting point, the specific heat remained constant 1126 J/kg.K. The boiling temperature was about 3808 K. The constant density and Poisson's ratio were used as 4440 kg/m^3 and 0.32 respectively [11]. The temperature dependent thermal and mechanical properties of Ti6Al4V alloy are given in Fig. 3 and Fig. 4 [11,40].

Al$_2$O$_3$ and TiC were deposited on the surface of Ti6Al4V substrate material. In this work, samples were named as Al$_2$O$_3$/Ti6Al4V and TiC/Ti6Al4V. Temperature independent material properties of Al$_2$O$_3$ and TiC are given in Table 2.

Laser Parameter, governing equation, and boundary condition

The influence of Laser parameters and heat flux distribution of the source is significant to develop a robust model. Laser parameters including beam radius, input Laser power and scanning speed were
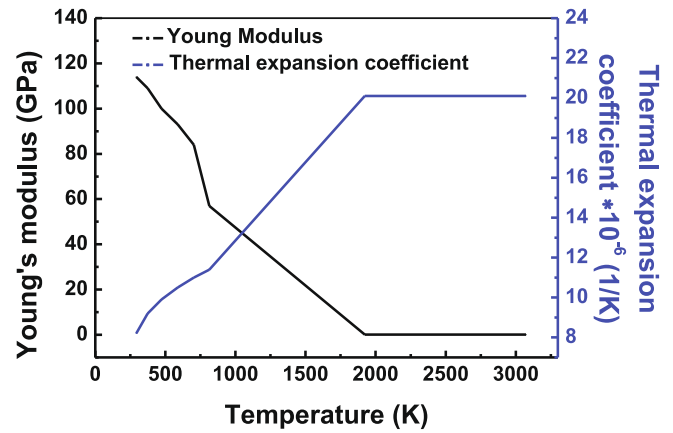
(a)
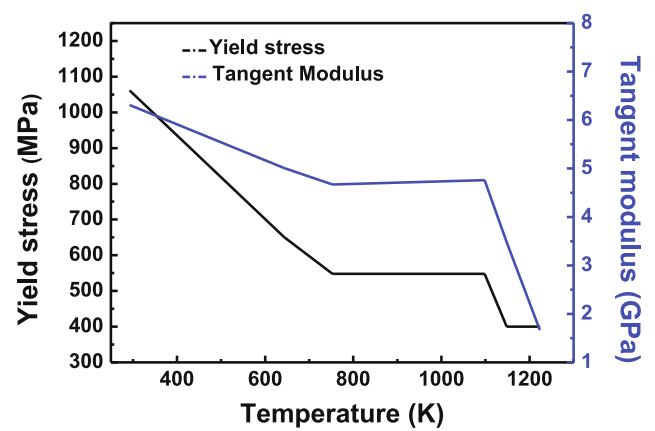
(b)

Fig. 4. Temperature dependent mechanical properties (a) Young's modulus and thermal expansion coefficient and (b) yield stress and tangent modulus of Ti6Al4V alloy used in this model.

Table 2
Thermo-mechanical properties of Al$_2$O$_3$ [41] and TiC [42] materials.

	Property	Units	Al$_2$O$_3$	TiC
Thermal material properties	Density	kg/m^3	3980	4940
	Specific Heat	J/kg-K	955	781.66
	Thermal conductivity	W/m-K	38.5	30.93
	Thermal expansion coefficient	K^{-1}	10.9	7.7×10^{-6}
	Melting temperature	K	2369	3338
Mechanical material properties	Young's modulus	GPa	413	451
	Poisson's ratio	–	0.33	0.19

taken from the experimental results. It is reported that the beam radius varied throughout the experiment along the scanning direction [11]. The beam radius was used as a tuning parameter in this simulation. Therefore, a parametric study was conducted with variable beam radius to optimise the Laser power. The optimised ranges of beam radius and Laser power were found respectively 0.7 to 0.8 mm and 550 to 650 W. The scanning speed was kept constant at 700 mm/min. This work used a 3D volumetric spherical Gaussian heat distribution expressed in Equation (2) to predict the temperature distribution [1].

$$Q_{(X,Y,Z)} = \frac{6\eta P}{\pi\sqrt{\pi}R^3} \exp^{(-3r2/R2)} \tag{2}$$

where, P was the power of laser beam, R was the laser beam radius, η was the absorption coefficient of material and $r = \sqrt{X^2 + Y^2 + Z^2}$ was the distribution of heat source. X, Y and Z were the three dimensions of a Cartesian coordinate system.

In thermal model, the classical heat conduction theory was applied to predict temperature distributions. The material properties of the clad and the substrate were assumed isotropic. The interaction of liquid metal was ignored as solidification happened within a fraction of a second. The phenomena of chemical reaction and stir convection in the melt pool was also ignored. The Governing equations of the 3D transient heat conduction model is expressed in Equation (3) [1],

$$\frac{\rho\partial(C_P T)}{\partial t} = \frac{\partial^2(kT)}{\partial x^2} + \frac{\partial^2(kT)}{\partial y^2} + \frac{\partial^2(kT)}{\partial z^2} + Q \tag{3}$$

where, ρ (kgm^{-3}) was the density, C_P (Jkg^{-1}K^{-1}) was the specific heat, t (s) was the time, T was the time dependent temperature and k (Wm^{-1}K^{-1}) was the thermal conductivity. X, Y and Z were the dimensions of the global coordinate system. Q was the Laser heat input. The initial temperature was set to room temperature, 293 K at the beginning of the process. The combined heat loss due to convection and radiation of the Laser beam was applied on the surface of the model according to the ref. [11]. A volumetric Gaussian heat flux (Q) was applied to deposit the clad material on the substrate. The absorption coefficient of Ti6Al4V was 0.25 [11].

For structural analysis, the transient nodal temperatures from the previous thermal analysis were transferred as static temperature load in every corresponding node. The same mesh was used for the structural analysis. The governing equation of predicting strain in the process is shown in Equation (4) [1],

$$\varepsilon = \varepsilon^{th} + \varepsilon^{el} + \varepsilon^{pl}, \tag{4}$$

where, $\varepsilon^{el}, \varepsilon^{pl}, \varepsilon^{th}$ were elastic, plastic, thermal strain, respectively. The substrate was assumed as stress free condition before starting the process as expressed in Equations (5) and (6). The bottom surface was constrained to zero displacement in all directions. The indirect coupling of thermo-structural analysis was assigned.

At t = 0,

$$\sigma(X, Y, Z) = 0 \tag{5}$$

$$\varepsilon(X, Y, Z) = 0 \tag{6}$$

Modelling of laser cladding process/direct energy process has been developed in three different sections such as powder flow dynamics, heat transfer in melt pool and clad properties. Therefore, the current work was focused on only hear transfer in melt pool section and applied laser process parameters which are required to develop this thermomechanical model.

Results and discussion

The thermo-mechanical simulation of laser cladding process has been performed to predict the temperature distribution and the residual stress distribution for deposition of similar and ceramic powder deposition on the titanium alloy. In Section "3D temperature and residual stress distribution", 3D temperature and residual stress distribution of Ti6Al4V alloy on Ti6Al4V alloy substrate has been explained. The verification of the current model has been done comparing with an established model in the literature which was validated by experiment. Finally, the verified model has been used to deposit ceramic materials on Ti6Al4V alloy to predict temperature and residual stress distribution.
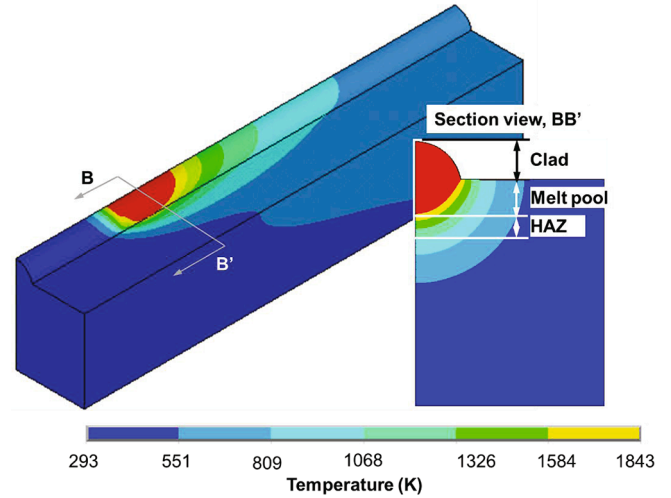

Fig. 5. The temperature distribution of the 3D model at 1.339 s. Power = 600 W, beam diameter = 0.7 mm and scanning speed = 700 mm/s, and section view BB'.
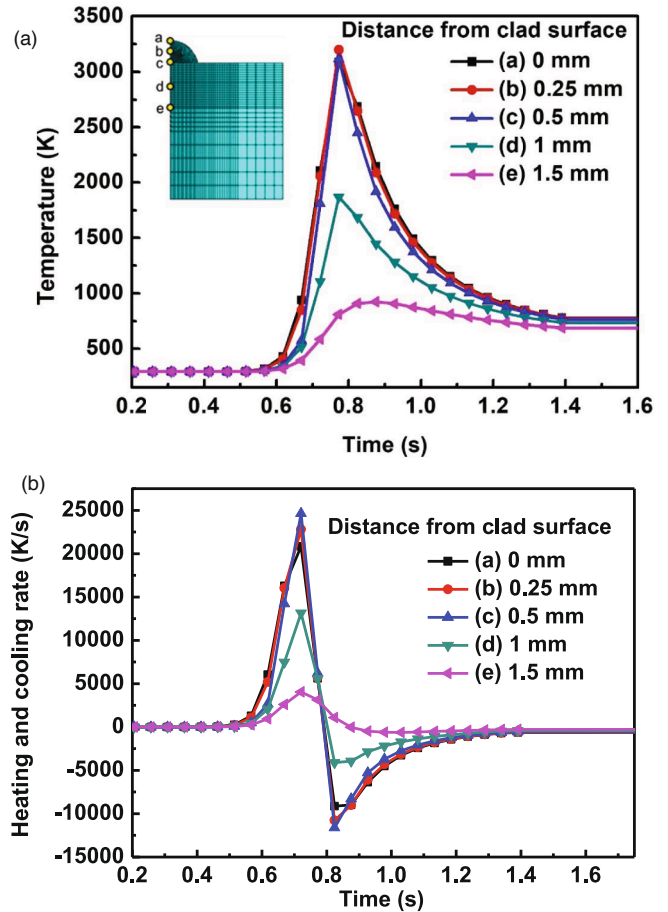

Fig. 6. (a) Temperature distribution at five positions along the depth and (b) heating and cooling rate at these positions.

3D temperature and residual stress distribution

Temperature distribution

Fig. 5 shows the isothermal distribution in a single track of the LC model for the laser power of 600 W, scanning speed of 700 mm/s and
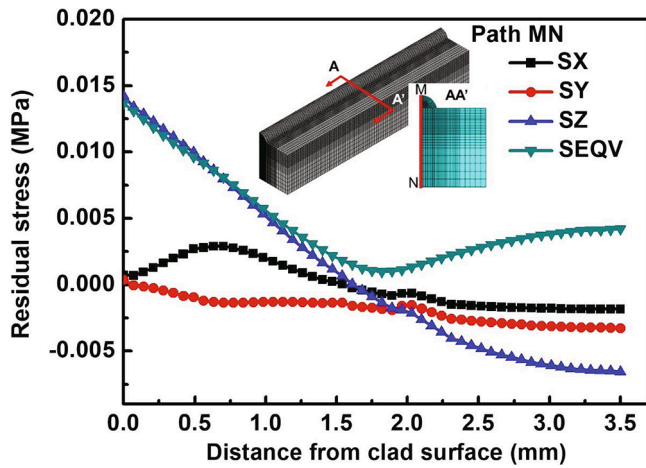
Fig. 7. The residual stresses distribution at the path MN, from the top of the clad surface to the bottom of the substrate.
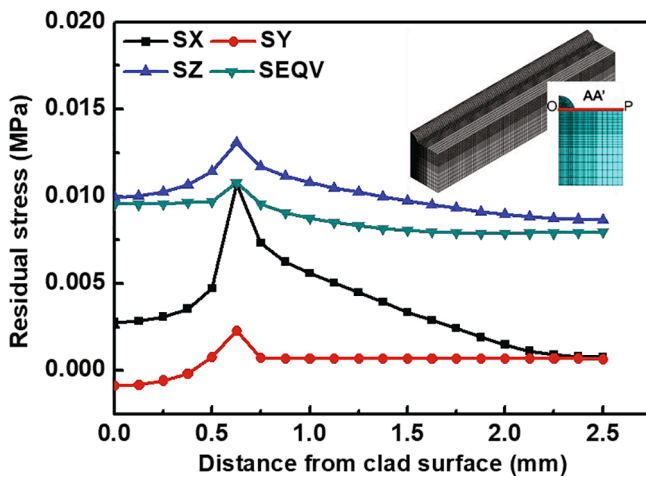

Fig. 8. The residual stress distribution at the path OP, from the symmetry plane to the right end of the substrate.

laser beam radius of 0.7 mm after 1.339 s. From the temperature profile, we can observe the shape and distribution of the heat-affected area such as the clad zone, melt pool and HAZ. Ti6Al4V alloy has a mushy zone where the solidus temperature is ~1843 K, and the liquidus temperature is ~1941 K [11]. In this figure, the range of temperature scale bar is kept up to solidus temperature 1843 K as the melting starts at this temperature. The deposited material over the substrate was considered as the clad region. The total melt pool area consisted of the clad and a part of the substrate area, where the material temperature was higher than the solidus temperature [25]. Similarly, the HAZ zone was designated where the temperature remained higher than the β transus temperature (1287 K) of Ti6Al4V alloy [43].

The heating cycles and cooling cycles at points a, b, c, d and e are given in Fig. 6(b). The heating rate (2.45 × 10^4 K/s) at location c (at the interface) was maximum as the heat source was applied at the interface of the clad and the substrate. The cooling rate at a, b and c locations were similar while at location d, the cooling rate was comparatively low [44]. The cooling rate at location c was 1.1 × 10^4 K/s. During solidification, liquid materials from point a to c pass the solidus temperature (1843 K), β transus temperature (1288 K) and martensitic transformation temperature (~1073 K) and finally, produce the acicular α' martensite [45-47]. The material in HAZ reaches above the β transus temperature (1267 K) and results in fine Widmanstatten structure [43]. Finally, the location which is below martensitic transformation temperature (~1073 K) will have the same microstructure of primary substrate phase before heat treatment.

Residual stress distribution for 3D Ti6Al4V model

One of the important applications of Ti6Al4V material is high temperature applications such as blades for aircraft turbines and steam turbine which goes through thermal stresses, local loading and cyclic loading. So, the stress state in these components is very crucial especially when the surface of these component is treated by laser heat source. Fig. 7 shows the residual stress distribution in X (SX), Y (SY) and Z (SZ) directions at the path MN for understanding of the nature of stresses in the clad and near surface of the substrate. The tensile residual stresses were found in X and Z directions for all samples. Tensile stress in X direction was increased from the clad surface to substrate and turned to compressive after 1.54 mm. In Z direction, maximum stress was generated at the top of the clad, then decreased inside the substrate. However, stress in Y direction was compressive as displacement constrain was applied in this direction.

Fig. 8 shows the residual stress distribution in X (SX), Y (SY) and Z (SZ) directions at the path OP. It shows that tensile residual stress formed in X and Z direction. Tensile stresses in both directions were increased from the symmetry plane to the end of the clad. Maximum stresses in all direction were in the substrate at 0.6 mm away from the symmetry plane. The equivalent stresses (SEQV) in path MN and OP were predicted to observe that the stress concentration in the clad did not exceed the yield strength of Ti6Al4V material. The maximum tensile residual stress (51.4 MPa) formed at the end of the clad which is much below than the yield strength (1100 MPa) of Ti6Al4V material. Therefore, there will be no crack formation or growth of cracks in this sample after cladding.
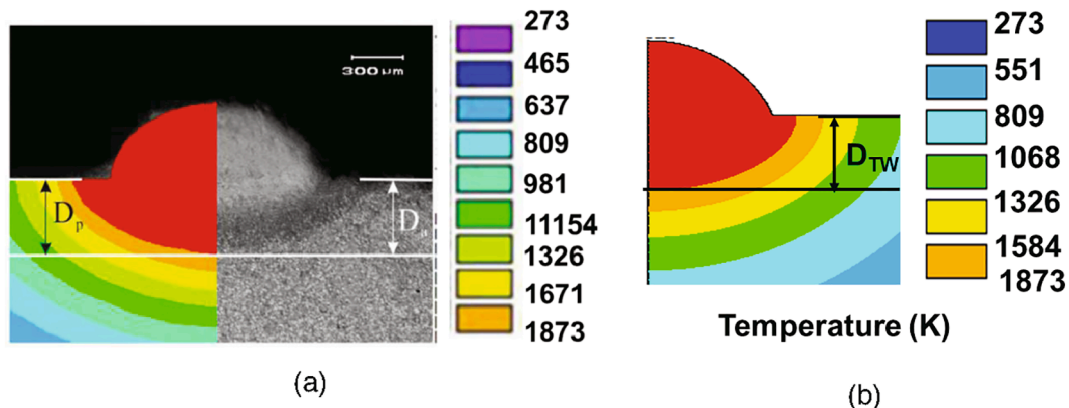

Fig. 9. The melt pool depth of (a) modelling and experimental results by Hao et al. and (b) current work by author.

Table 3

Comparison of predicted results between the model of Hao et al. and the current model.

Condition	Predicted results by Hao et al. [11]	Predicted results from the current model	% difference
Peak temperature	3200 K	3168 K	1.9
Melt pool depth at the centre of clad	0.41 mm	0.406 mm	0.97

Table 4

Laser parameters for deposition of Al_2O_3/Ti6Al4V and TiC/Ti6Al4V samples [48].

Laser Parameters	Units	Laser type	Al_2O_3	TiC
Absorption coefficient	–	Fiber	0.03	0.82
		CO_2	0.96	0.46
Laser travel speed	mm/s	–	700	700
Optimised process parameters in current work				
Beam diameter	mm	–	0.7	0.7
laser power	W	Fiber	8000	380
		CO_2	250	675

Verification of the model

The verification of the model has been done based on the previously established model, which was validated by experimental works. The simulated work by Hao et al. was taken to perform the benchmark [11] where laser beam radius was modified iteratively according to the difference between the melt pool depth from experimental samples and predicted melt pool boundary. The dimension of heat source does not remain constant during experiments. Therefore, there is no physical relation between the actual heat source radius and implemented radius in their model. In this work, the model has been developed using same process parameters and given dimensions in their published work. The laser beam radius was optimised iteratively based on the melt pool depth. As the spherical volumetric heat source could not produce exact shape of the melt pool, the distribution of the heat source was optimised to obtain the required shape of the melt pool.

The predicted peak temperature by the author is 62 K lower than the developed model by Hao et al. which results in 1.9% deviation. The difference of temperature could be the reason of differences in materials properties, number of sub steps, iteration number, the iterative value of laser heat source diameter, the distribution of heat source and the position of heat source. Additionally, Hao et al. validated the predicted results with experimental results, shown in Fig. 9.

The simulated melt pool depth (0.41 mm) and the actual melt pool depth (from experiments) (da = 0.41 mm) are same. In this work, the depth of melt pool was found 0.406 mm which is very near the results reported by Hao et al. The predicted results of this current work and the developed model of Hao et al. are summarised in Table 3. From this analysis, it can be understood that the technique of mesh and boundary conditions are used to develop the model is good enough to use for further analysis.

Case studies with dissimilar material systems

Two ceramic materials, Al_2O_3 and TiC, were chosen to understand the thermal and residual stresses during the deposition on Ti6Al4V substrate. To deposit ceramic materials using laser heat source, it is essential to understand their response/absorptivity to different laser sources as the material absorptivity depends on the wavelength of laser. For examples, the absorptivity of Ti6Al4V, Al_2O_3 and TiC are 0.25, 0.03 and 0.82 respectively for fiber laser which has wavelength around 1.06 μm [48]. On the other hand, the absorptivity of these materials for CO_2 laser (10.6 μm) are different. For CO_2 laser, the absorptivity of Al_2O_3 and
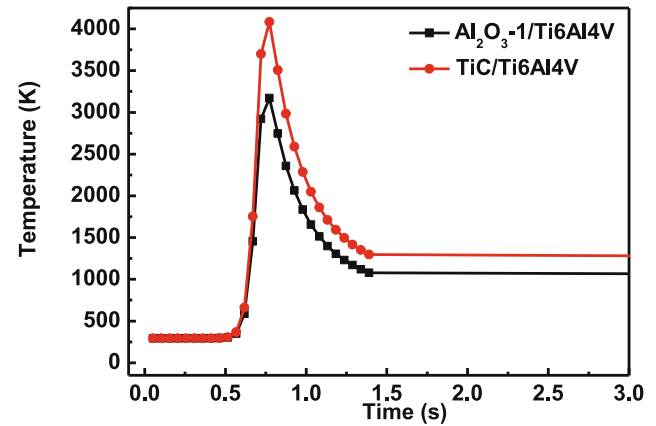

Fig. 10. The transient temperature distribution of Al_2O_3/Ti6Al4V and TiC/Ti6Al4V samples.

TiC are 0.96 and 0.46, respectively [48]. Hence, the required power to achieve the same heat density to melt the desired materials can vary. In this work, it was found that to get a perfectly molten clad of Al_2O_3 on the Ti6Al4V substrate, fiber laser (1.06 μm) required 8000 W. For CO_2 laser (10.6 μm), it was 250 W due to the different absorptivity of the two laser heat sources. Similarly, TiC cladding material required 380 W for fiber laser and 675 W for CO_2 laser. All these models were developed using 1.4 mm beam diameter which can alter the required laser power. All observation for Al_2O_3 and TiC deposited samples for different wavelength lasers are given in Table 4.

Fig. 10 shows the temperature evolution at the interface of the clad and the substrate during the LC process for Al_2O_3/Ti6Al4V and TiC/Ti6Al4V samples. The predicted temperature profile offers the formation time of the melt pool and peak temperature at the clad and the substrate interface. The peak temperature at the interface was 3170 K and 4082 K for Al_2O_3/Ti6Al4V and TiC/Ti6Al4V samples, respectively. In both cases, the peak temperatures were above the melting temperature, which ensured the melting of the clad materials. However, the peak temperature of TiC/Ti6Al4V is 4082 K goes above the vaporisation temperature of Ti6Al4V alloy (3808 K), which evaporates a few micrometers (2–3 μm) from the substrate surface. The current model assumed that 2–3 μm substrate material loss will be insignificant compared to 450–500 μm clad. During multi-pass cladding, the loss of substrate material at the corner of the clad will be covered by next clad deposition with 20–30% overlapping.
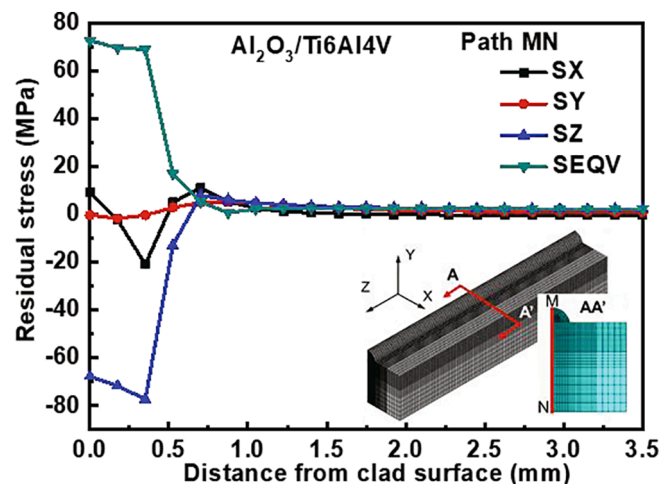

Fig. 11. The residual stresses distribution of Al_2O_3/Ti6Al4V along the path MN.

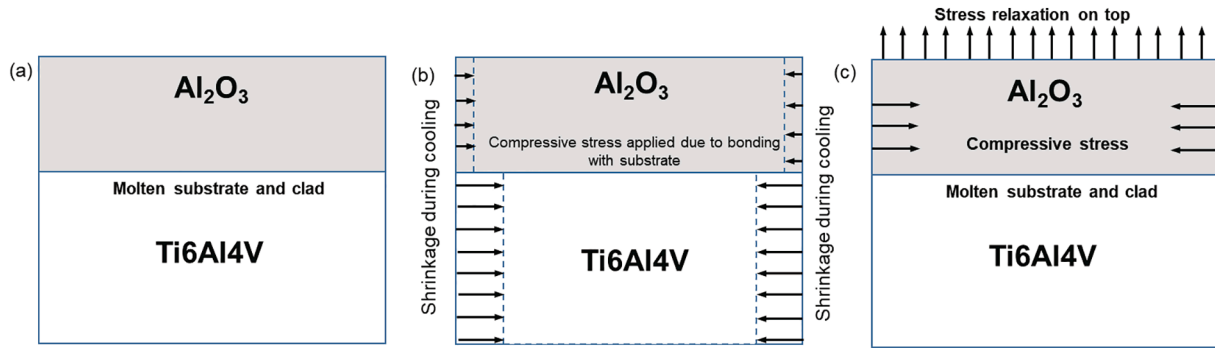**Fig. 12.** Schematic diagram to explain the generation of compressive stress in the clad of Al$_2$O$_3$/Ti6Al4V sample along the path MN.

Z. Fan et al. predicted cooling rate of Al$_2$O$_3$ deposition during selective laser melting was 7.038×10^3 K/s resulted in columnar and equiaxial dendrites microstructure [49]. The predicted cooling rate of Al$_2$O$_3$/Ti6Al4V sample was 6.6×10^3 K/s which was near to the cooling rate proposed by Z. Fan et al. [49]. Therefore, we can assume the microstructure in this system will be columnar and equiaxial dendrites in the Al$_2$O$_3$ clad [29]. In the Ti6Al4V substrate, the cooling rate was 6.6×10^3 K/s which can form α' martensite in the melt pool. HAZ material reaches above the β transus temperature (1267 K) and results in fine Widmanstatten structure [43]. Finally, the location which is below martensitic transformation temperature (~1073 K) will have the same microstructure of the primary substrate phase. S. Liu et al. reported that the dendritic structure was formed for deposition of TiC during selective laser melting when the predictive cooling rate was 10^4 K/s [50]. In the current work, the cooling rate of TiC/Ti6Al4V sample was 1.1×10^4 K/s which is almost same as the reported cooling rate by S. Liu et al. This ensures the formation of dendritic structure in the clad. In substrate material, the microstructure will be as same as the sample in Al$_2$O$_3$/Ti6Al4V.

Fig. 11 shows the residual stresses distribution of the Al$_2$O$_3$/Ti6Al4V sample at the path MN. In the clad, the predicted residual stresses in X, Y and Z directions along the path MN were mainly compressive in nature except stress at the top surface of the clad in the X direction. The compressive nature of the clad can be explained based on the concept of the mismatch of thermal strain [31]. Thermal strain is the multiplication of thermal expansion coefficient and temperature difference between room temperature and raised temperature. The mismatch of thermal strain is one of the key reasons of the generation of the residual stress mentioned in the author's previous analytical model [31]. During the LC process, the temperature of the near surface of the substrate goes up to the same temperature of the clad material. So, the temperature difference between the room temperature and raised temperature of the clad and the near surface of the substrate is almost similar. Therefore, the mismatch of thermal strain at the interface is highly dependent on the thermal expansion coefficient of the clad and the substrate material. During deposition, Al$_2$O$_3$ spreads over the surface of Ti6Al4V substrate and forms metallurgical bonding. Al$_2$O$_3$ has a higher thermal expansion coefficient than Ti6Al4V. Therefore, during cooling Ti6Al4V substrate material shrinks more than Al$_2$O$_3$. As Ti6Al4V substrate material shrinks more than Al$_2$O$_3$ clad and creates metallurgical bonding with the clad, it applies compressive stresses in the clad shown in Fig. 12 (b). Finally, the expanded clad remains as compressed by the substrate material. So, the clad experiences the compressive stress after cooling down to room temperature.

The reason for the formation of tensile stress in the X direction at the top surface of the clad can be explained based on strain and Poisson's ratio concept. The material at the top surface of the clad has no material constrain. As the clad material is in compression by the substrate material at the interface, it allows some relaxation by expanding on the top, which causes positive strain, shown in Fig. 12 (c). This positive strain
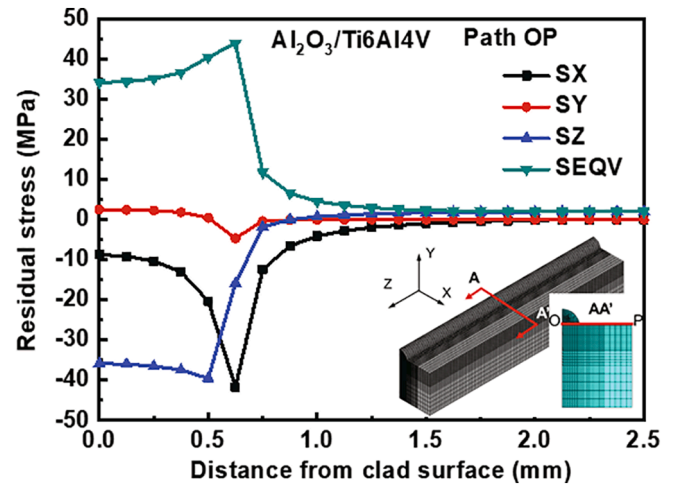

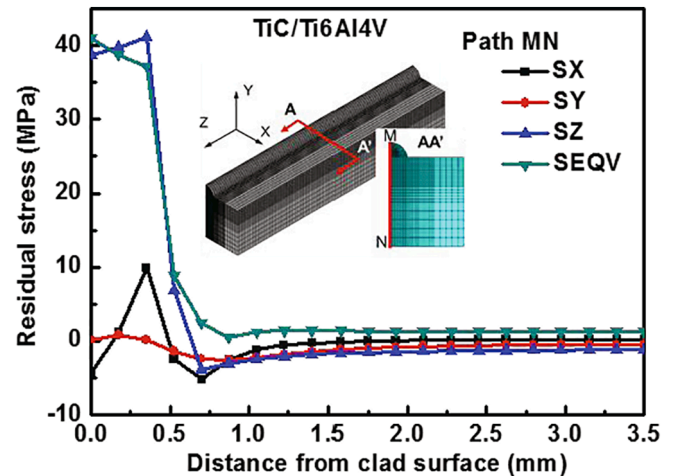**Fig. 13.** The residual stresses distribution of Al$_2$O$_3$/Ti6Al4V along the path OP.

Fig. 14. The residual stresses distribution of TiC/Ti6Al4V along the path MN.

results in tensile stress on the top clad surface.

The predicted residual stress in path OP of Al$_2$O$_3$/Ti6Al4V sample are compressive in X, Y and Z directions shown in Fig. 13. This phenomenon can be similarly explained based on the concept described above. The predicted von-Mises stress (SEQV) (72.7 MPa) is lower than the yield stress of Ti6Al4V and the tensile strength of Al$_2$O$_3$ ensures no yielding in the Al$_2$O$_3$/Ti6Al4V sample.

Fig. 14 shows the residual stresses distribution of TiC/Ti6Al4V sample at the path MN. In the clad, the predicted residual stresses in X, Y
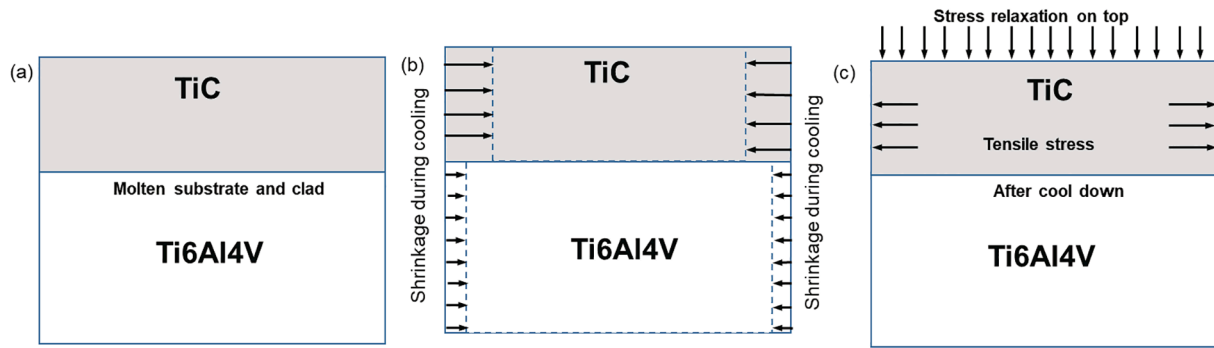
Fig. 15. Schematic diagram to explain the generation of tensile stress in the clad of TiC/Ti6Al4V sample.
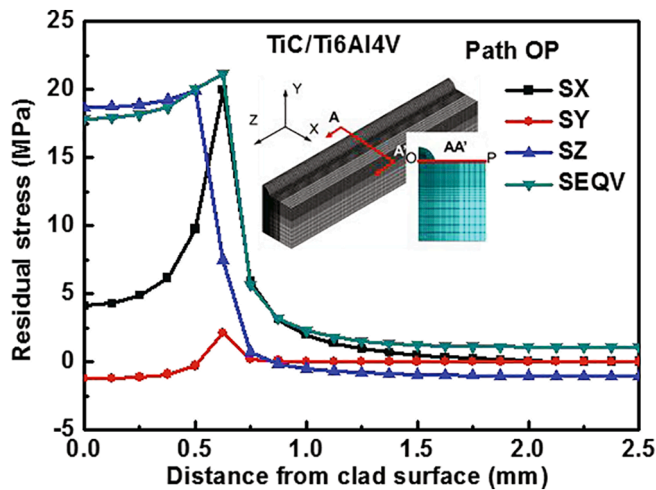

Fig. 16. The residual stresses distribution of TiC/Ti6Al4V along the path OP.

and Z directions along the path MN are mainly tensile in nature except stress at the top surface of the clad in X direction. The material at the top surface of the clad in X direction experiences compressive stress.

During deposition TiC spreads over the surface of Ti6Al4V and develops metallurgical bonding. As, TiC has lower thermal expansion coefficient than Ti6Al4V, it starts shrinking more than Ti6Al4V. However, due to metallurgical bonding / substrate material constrain, TiC cannot shrink and comes back to original position at the room temperature. It stays expanded by the force / material constrain from substrate material which causes tensile stresses in the TiC clad, shown in Fig. 15.

The material at the top surface of the clad has no material constrain. As the clad material is in tensile stress, it allows some relaxation by contracting on the top which causes negative strain, shown in Fig. 16. This negative strain results in the compressive stress on the top clad surface. The predicted residual stress of TiC/Ti6Al4V sample in path OP were tensile in X, Y and Z directions shown in Fig. 16. The predicted maximum equivalent stress (SEQV, 41.03 MPa) is lower than the yield stress of Ti6Al4V and the tensile strength of TiC. However, the nature of residual stresses is tensile. Therefore, it is important to consider that the actual yield/tensile stress under stressed condition may not be same as the theoretical value. The displacement constrain was applied in Y direction. So, material in Y direction was always restricted to expand which generated mainly compressive stress in Y direction for all samples.

Conclusions

A 3D finite element transient thermomechanical model of the Laser Cladding process was successfully developed using the ANSYS

multiphysics software. Ti6Al4V alloy was used for both the clad and the substrate materials. This thermomechanical model is verified with an established finite element model of LC that was validated experimentally. Upon verification, the deviation in the predicted results of the developed model and the existing model was found 1.9%. Additionally, two ceramic clad materials, Al_2O_3 and TiC, with Ti6Al4V substrate were used in this model to study the effect of the different clad materials on the residual stress in the system that implied the compatibility between the clad materials and substrate for the process. These models can be used to predict the three-dimensional temperature and residual stress distribution. The predicted heating and cooling rates can be utilised to estimate possible microstructure in the clad and the substrate. The deposition of Ti6Al4V alloy introduced 51.4 MPa tensile stress in the clad below the yield strength of (1100 MPa) of Ti6Al4V material, hence, confirms no crack formation or growth of cracks during operation. By utilising different ceramic clad materials, the model showed that Al_2O_3 induced compressive stress whereas TiC stored tensile stress both in the clad and interface. Hence, the use of Al_2O_3 instead of TiC as cladding material on Ti6Al4V substrate reduced crack formation tendency. Therefore, Al_2O_3 is more compatible than TiC to deposit on the Ti6Al4V substrate by LC.

Declaration of Competing Interest

The authors declare that they have no known competing financial interests or personal relationships that could have appeared to influence the work reported in this paper.

References

[1] N. Tamanna, R. Crouch, S. Naher, Progress in numerical simulation of the laser cladding process, Opt. Lasers Eng. 122 (2019) 151–163, https://doi.org/10.1016/j.optlaseng.2019.05.026.

[2] E. Toyserkani, A. Khajepour, S.F. Corbin, Laser Cladding, 1st ed, CRC Press, USA, 2004.

[3] I. Tabernero, A. Lamikiz, E. Ukar, L.N. López de Lacalle, C. Angulo, G. Urbikain, Numerical simulation and experimental validation of powder flux distribution in coaxial laser cladding, J. Mater. Process. Technol. 210 (15) (2010) 2125–2134, https://doi.org/10.1016/j.jmatprotec.2010.07.036.

[4] P. Nie, O.A. Ojo, Z. Li, Modeling analysis of laser cladding of a nickel-based superalloy, Surf. Coatings Technol. 258 (2014) 1048–1059, https://doi.org/10.1016/j.surfcoat.2014.07.030.

[5] W. Ya, B. Pathiraj, S. Liu, 2D modelling of clad geometry and resulting thermal cycles during laser cladding, J. Mater. Process. Technol. 230 (2016) 217–232, https://doi.org/10.1016/j.jmatprotec.2015.11.012.

[6] C.-F. Hung, J. Lin, Solidification model of laser cladding with wire feeding technique, J. Laser Appl. 16 (3) (2004) 140–146, https://doi.org/10.2351/1.1771167.

[7] H.E. Cheikh, B. Courant, 3D Finite Element Simulation to Predict the Induced Thermal Field in Case of Laser Cladding Process and Half Cylinder Laser, Clad 1 (2012) 55–59.

[8] P. Farahmand, R. Kovacevic, An experimental–numerical investigation of heat distribution and stress field in single- and multi-track laser cladding by a high-power direct diode laser, Opt. Laser Technol. 63 (2014) 154–168, https://doi.org/10.1016/j.optlastec.2014.04.016.

[9] P. Farahmand, P. Balu, F. Kong, R. Kovacevic, Investigation of Thermal Cycle and Hardness Distribution in the Laser Cladding of AISI H13 tool steel produced by a High Power Direct Diode Laser, in: Proc. ASME 2013 Int. Mech. Eng. Congr. Expo., Callifornia, USA, 2015: pp. 1–12.

[10] L.F. Guo, T.M. Yue, H.C. Man, A finite element method approach for thermal analysis of laser cladding of magnesium alloy with preplaced Al–Si powder, J. Laser Appl. 16 (4) (2004) 229–235, https://doi.org/10.2351/1.1809634.

[11] M. Hao, Y. Sun, A FEM model for simulating temperature field in coaxial laser cladding of TI6AL4V alloy using an inverse modeling approach, Int. J. Heat Mass Transf. 64 (2013) 352–360, https://doi.org/10.1016/j.ijheatmasstransfer.2013.04.050.

[12] J.T. Hofman, D.F. de Lange, B. Pathiraj, J. Meijer, FEM modeling and experimental verification for dilution control in laser cladding, J. Mater. Process. Technol. 211 (2) (2011) 187–196, https://doi.org/10.1016/j.jmatprotec.2010.09.007.

[13] Y. Lei, R. Sun, J. Lei, Y. Tang, W. Niu, A new theoretical model for high power laser clad TiC/NiCrBSiC composite coatings on Ti6Al4V alloys, Opt. Lasers Eng. 48 (9) (2010) 899–905, https://doi.org/10.1016/j.optlaseng.2010.03.016.

[14] W.C. Tseng, J.N. Aoh, Simulation study on laser cladding on preplaced powder layer with a tailored laser heat source, Opt. Laser Technol. 48 (2013) 141–152, https://doi.org/10.1016/j.optlastec.2012.09.014.

[15] N. Tamanna, I.R. Kabir, S. Naher, A numerical investigation of similar and dissimilar clad materials on H13 steel substrate in the Laser Cladding process ABSTRACT, (2019) 1–9.

[16] Y. Chew, J.H.L. Pang, G. Bi, B. Song, Thermo-mechanical model for simulating laser cladding induced residual stresses with single and multiple clad beads, J. Mater. Process. Technol. 224 (2015) 89–101, https://doi.org/10.1016/j.jmatprotec.2015.04.031.

[17] I.A. Roberts, Investigation of residual stresses in the Laser Melting of metal powders in additive layer, (2012).

[18] M. Eslami, R. Hetnarski, J. Ignaczak, N. Noda, N. Sumi, Theory of elasticity and thermal stresses, 1st ed., Waterloo, Canada, 2013 http://link.springer.com/content/pdf/978-94-007-6356-2.pdf.

[19] R. Parekh, R.K. Buddu, R.I. Patel, Multiphysics simulation of laser cladding process to study the effect of process parameters on clad geometry, Procedia Technol. 23 (2016) 529–536, https://doi.org/10.1016/j.protcy.2016.03.059.

[20] P. Farahmand, R. Kovacevic, Laser cladding assisted with an induction heater (LCAIH) of Ni-60%WC coating, J. Mater. Process. Technol. 222 (2015) 244–258, https://doi.org/10.1016/j.jmatprotec.2015.02.026.

[21] X. He, G. Yu, J. Mazumder, Temperature and composition profile during double-track laser cladding of H13 tool steel, J. Phys. D. Appl. Phys. 43 (1) (2010) 015502, https://doi.org/10.1088/0022-3727/43/1/015502.

[22] Y. Lee, D.F. Farson, Simulation of transport phenomena and melt pool shape for multiple layer additive manufacturing, J. Laser Appl. 28 (1) (2016) 012006, https://doi.org/10.2351/1.4935711.

[23] L. Chen, Y.u. Zhao, B. Song, T. Yu, Z. Liu, Modeling and simulation of 3D geometry prediction and dynamic solidification behavior of Fe-based coatings by laser cladding, Opt. Laser Technol. 139 (2021) 107009, https://doi.org/10.1016/j.optlastec.2021.107009.

[24] B. Song, T. Yu, X. Jiang, W. Xi, X. Lin, The relationship between convection mechanism and solidification structure of the iron-based molten pool in metal laser direct deposition, Int. J. Mech. Sci. 165 (2020) 105207, https://doi.org/10.1016/j.ijmecsci.2019.105207.

[25] X. Lu, M. Cervera, M. Chiumenti, J. Li, X. Ji, G. Zhang, X. Lin, Modeling of the Effect of the Building Strategy on the Thermomechanical Response of Ti-6Al-4V Rectangular Parts Manufactured by Laser Directed Energy Deposition, (n.d.).

[26] M. Krzyzanowski, S. Bajda, Y. Liu, A. Triantaphyllou, W.M. Rainforth, M. Glendenning, M. Krzyzanowski, S. Bajda, Y. Liu, 3D analysis of thermal and stress evolution during laser cladding of bioactive glass coatings, J. Mech. Behav. Biomed. Mater. 59 (2016) 404–417, https://doi.org/10.1016/j.jmbbm.2016.02.023.

[27] D. Youssef, S. Hassab-Elnaby, S.R. Al-Sayed, New 3D model for accurate prediction of thermal and microstructure evolution of laser powder cladding of Ti6Al4V alloy,

Alexandria Eng. J. 61 (5) (2022) 4137–4158, https://doi.org/10.1016/j.aej.2021.09.014.

[28] C. Wang, J. Li, T. Wang, L. Chai, C. Deng, Y. Wang, Y. Huang, Microstructure and properties of pure titanium coating on Ti-6Al-4V alloy by laser cladding, Surf. Coatings Technol. 416 (2021) 127137, https://doi.org/10.1016/j.surfcoat.2021.127137.

[29] Y. Chen, D. Wu, G. Ma, W. Lu, D. Guo, Coaxial laser cladding of Al2O3-13%TiO2 powders on Ti-6Al-4V alloy, Surf. Coatings Technol. 228 (2013) S452–S455, https://doi.org/10.1016/j.surfcoat.2012.05.027.

[30] JET-HOT COATINGS, Jet-Hot.Com. (n.d.). https://www.jet-hot.com/coatings (accessed February 26, 2022).

[31] N. Tamanna, R. Crouch, I.R. Kabir, S. Naher, An analytical model to predict and minimize the residual stress of laser cladding process, Appl. Phys. A. 124 (2018) 202, https://doi.org/10.1007/s00339-018-1585-6.

[32] A. Mthisi, A.P.I. Popoola, D.I. Adebiyi, O.M. Popoola, Laser Cladding of Ti-6Al-4V Alloy with Ti-Al2O3 Coating for Biomedical Applications, IOP Conf. Ser. Mater. Sci. Eng. 350 (2018) 012005, https://doi.org/10.1088/1757-899X/350/1/012005.

[33] J. Qian, J. Zhang, S. Li, C. Wang, Study on Laser Cladding NiAl/Al2O3 Coating on Magnesium Alloy, Rare Met. Mater. Eng. 42 (3) (2013) 466–469, https://doi.org/10.1016/S1875-5372(13)60049-1.

[34] X. Luo, Z. Yao, P. Zhang, D. Gu, Al2O3 nanoparticles reinforced Fe-Al laser cladding coatings with enhanced mechanical properties, J. Alloys Compd. 755 (2018) 41–54, https://doi.org/10.1016/j.jallcom.2018.04.266.

[35] H. Chen, Y. Lu, Y. Sun, Y. Wei, X. Wang, D. Liu, Coarse TiC particles reinforced H13 steel matrix composites produced by laser cladding, Surf. Coatings Technol. 395 (2020) 125867, https://doi.org/10.1016/j.surfcoat.2020.125867.

[36] W. Application, Laser Deposition of Titanium Oxide on Titanium Alloy for, (2020).

[37] Y. Sun, M. Hao, Statistical analysis and optimization of process parameters in Ti6Al4V laser cladding using Nd:YAG laser, Opt. Lasers Eng. 50 (7) (2012) 985–995, https://doi.org/10.1016/j.optlaseng.2012.01.018.

[38] I.R. Kabir, D. Yin, N. Tamanna, S. Naher, Thermomechanical modelling of laser surface glazing for H13 tool steel, Appl. Phys. A Mater. Sci. Process. 124 (3) (2018), https://doi.org/10.1007/s00339-018-1671-9.

[39] I.R. Kabir, D. Yin, S. Naher, 3D thermal model of laser surface glazing for H13 tool steel, in: 20th Int. ESAFORM Conf. Mater. Form., 2017: p. 130003. https://doi.org/10.1063/1.5008152.

[40] E.R. Delinger, Thermo-mechanical model development and experimental validation for metallic parts in additive manufacturing, The Pennsylvania State University, 2015. PhD.

[41] Alumina AZOM, (2018). https://www.azom.com/properties.aspx?ArticleID=52 (accessed October 12, 2018).

[42] Titanium carbide, MEMSnet. (2017). https://www.memsnet.org/material/titaniumcarbideticbulk/ (accessed January 3, 2019).

[43] R. Cottam, M. Brandt, Laser cladding of Ti6Al4V powder on Ti6Al4V substrate: Effect of laser cladding parameters on microstructure, Phys. Procedia. 12 (2011) 323–329, https://doi.org/10.1016/j.phpro.2011.03.041.

[44] N. Tamanna, R. Crouch, S. Naher, A One-dimensional Analysis of the Distribution of Temperature, Stress and Strain in the co-axial Laser Cladding Process, 20th Int, ESAFORM Conf. Mater. Form. 040015 (2017).

[45] P. Barriobero-Vila, Effect of heat treatments on the microstructure of deformed Ti-6Al-4V, (2010) 69.

[46] J. Yang, H. Yu, J. Yin, M. Gao, Z. Wang, X. Zeng, Formation and control of martensite in Ti-6Al-4V alloy produced by selective laser melting, Mater. Des. 108 (2016) 308–318, https://doi.org/10.1016/j.matdes.2016.06.117.

[47] B. Vrancken, L. Thijs, J.P. Kruth, J. Van Humbeeck, Heat treatment of Ti6Al4V produced by Selective Laser Melting: Microstructure and mechanical properties, J. Alloys Compd. 541 (2012) 177–185, https://doi.org/10.1016/j.jallcom.2012.07.022.

[48] J.P. Kruth, X. Wang, T. Laoui, L. Froyen, Lasers and materials in selective laser sintering, Assem. Autom. 23 (2003) 357–371.

[49] Z. Fan, M. Lu, H. Huang, Selective laser melting of alumina: A single track study, Ceram. Int. 44 (8) (2018) 9484–9493, https://doi.org/10.1016/j.ceramint.2018.02.166.

[50] S. Liu, Y.C. Shin, Simulation and experimental studies on microstructure evolution of resolidified dendritic TiCx in laser direct deposited Ti-TiC composite, Mater. Des. 159 (2018) 212–223, https://doi.org/10.1016/j.matdes.2018.08.053.